

Synoptic formation of double tropopauses

Chengji Liu¹ and Elizabeth Barnes¹

¹Department of Atmospheric Sciences, Colorado State University, Fort Collins, Colorado, USA.

Key Points:

- Double tropopauses are closely linked to Rossby wave breaking.
- Double tropopauses can form as a result of differential advection and/or the destabilization of thermal stratification.
- The occurrence of double tropopauses substantially enhances stratosphere-troposphere exchange of air mass.

Abstract

Double tropopauses are ubiquitous in the midlatitude winter hemisphere and represent the vertical stacking of two stable tropopause layers separated by a less stable layer. By analyzing COSMIC GPS data, reanalysis, and eddy lifecycle simulations, we demonstrate that they often occur during Rossby wave breaking and act to increase the stratosphere-to-troposphere exchange of mass. We further investigate the adiabatic formation of double tropopauses and propose two mechanisms by which they can occur. The first mechanism operates at the tropopause break in the subtropics where the higher tropical tropopause sits on one side of the break and the lower extratropical tropopause sits on the other. The double tropopauses are then formed by differential meridional advection of the higher and lower tropopauses on the two sides of the tropopause break. We show that anticyclonic wave breaking can form double tropopauses mainly by providing stronger poleward advection of the higher tropopause in its poleward lobe. Cyclonic wave breaking mainly forms double tropopauses by providing stronger equatorward advection of the lower tropopause in its equatorward lobe. We demonstrate in the COSMIC GPS data and reanalysis that about half of the double tropopauses in the northern hemisphere winter can be directly attributed to such differential advection. For the second mechanism, adiabatic destabilization of the air above the tropopause contributes to the formation of a double tropopause. In this case, a tropopause inversion layer (TIL) is necessary for this destabilization to result in a double tropopause.

1 Introduction

The tropopause marks an interface between two dynamically and chemically distinct parts of the atmosphere – the stratosphere and the troposphere. The transport and mixing of compositions across this interface has profound consequences for the global climate and chemistry. For example, the variation in greenhouse gases such as water vapor and ozone near the tropopause is strikingly efficient in altering the radiative forcing and hence the global surface temperature [e.g. *Forster et al.*, 1997; *Solomon et al.*, 2010; *Riese et al.*, 2012]. Furthermore, the variability of stratosphere-to-troposphere ozone flux can translate to the variability of the health-related ultraviolet index [e.g. *Hegglin and Shepherd*, 2009]. In addition to its radiative impact, ozone is itself detrimental to human health and its surface concentration is currently regulated by the *U.S. Environmental Protection Agency (U.S.*

41 EPA) [2006] and the European Union as part of the European Commission’s Air Quality
42 Standards.

43 The structure of the tropopause is thus of great interest due to its ability to influ-
44 ence the exchange between the stratosphere and the troposphere. Particularly, the verti-
45 cal folding of the tropopause is an important candidate for enhancing this exchange [e.g.
46 Shapiro, 1980]. When observed via sounding profiles, this folding structure appears as
47 “double tropopauses” [e.g. Kochanski, 1955; Seidel and Randel, 2006], featuring the ver-
48 tical stacking of two stable tropopause layers separated by a less stable layer (Fig. 1a).
49 Double tropopauses occur in both hemispheres and all seasons, with their highest frequen-
50 cies in winter [e.g. Randel et al., 2007a; Añel et al., 2008; Peevey et al., 2012]. During
51 double tropopause events, radiosonde and satellite observations above the first tropopause
52 show less stratospheric trace gases and more tropospheric trace gases compared to single
53 tropopause events [e.g. Randel et al., 2007a; Schwartz et al., 2015], indicating strengthened
54 transport and mixing between the two tropopauses. However, to our knowledge no quan-
55 titative comparison has been done regarding the role of double tropopauses in enhancing
56 stratosphere-troposphere exchange. Quantitatively addressing this question is one of the
57 goals of this study.

58 The occurrence of double tropopauses has been shown to be associated with extrat-
59 ropical synoptic disturbances. Studies show an eastward propagation of double tropopauses
60 events in Hovmöller diagrams [e.g. Castanheira and Gimeno, 2011; Peevey et al., 2012],
61 indicating their association with baroclinic Rossby waves embedded in westerly flow. Peevey
62 et al. [2014] documented the linkage between double tropopauses and warm conveyor
63 belts, a common feature in baroclinic disturbances. Wang and Polvani [2011] demonstrated
64 in idealized simulations that it is the breaking of these waves that creates the largest cov-
65 erage of double tropopauses. In observations this linkage between Rossby wave breaking
66 and double tropopauses, however, has only been shown in individual case studies [e.g.
67 Pan et al., 2009; Homeyer et al., 2014]. In this work, we present the statistical relation-
68 ship between double tropopauses and synoptic Rossby wave breaking by applying a wave
69 breaking detection algorithm to satellite observations and reanalysis data.

70 The specific mechanisms responsible for the formation of double tropopauses re-
71 main unknown, despite the many clues alluded to in previous studies. The clues include
72 baroclinic wave activity and the tropopause inversion layer (TIL) [e.g. Wang and Polvani,

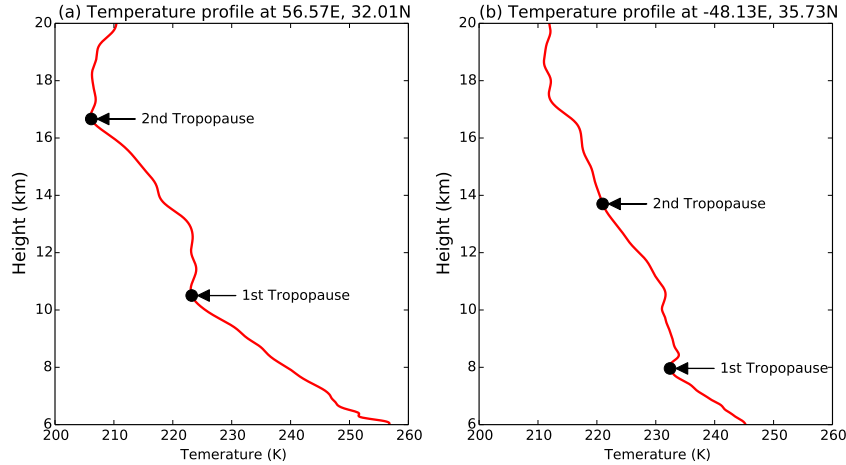


Figure 1. Temperature profiles from COSMIC GPS data on (a) Jan 24, 2007, and (b) Jan 22, 2007.

2011; Peevey *et al.*, 2014], which is a thin layer with very strong stratification right above the tropopause [e.g. Birner *et al.*, 2002; Birner, 2006]. Following these clues, we explore possible mechanisms with a focus on adiabatic synoptic processes. In particular, we propose that double tropopauses can be formed by either *advection* of existing tropopauses or *creation* of new tropopauses above old ones. We demonstrate these two mechanisms in satellite observation, reanalysis, and model simulations, and show how baroclinic waves and a TIL help form double tropopauses by advecting and creating tropopauses.

We address three questions in this study: (1) What are the statistical relationships between double tropopauses and Rossby wave breaking in the observations? (2) What are the mechanisms responsible for double tropopause formation? (3) How do double tropopauses impact stratosphere-troposphere exchange? The dataset and diagnostic methods used to address these questions are described in Section 2. Sections 3 to 5 address the three questions above in order. Section 6 summarizes the main conclusions and discusses how our results relate to those of previous studies.

2 Data and methodology

2.1 GPS radio occultation data

GPS radio occultation measurements (hereafter GPS data) provide accurate temperature observations with high vertical resolution [e.g. Liou *et al.*, 2007], which reveal finer and more realistic tropopause structure compared to reanalysis [e.g. Birner *et al.*, 2006;

93 *Son et al.*, 2011]. We use GPS data from the Constellation Observing System for Meteo-
 94 rology, Ionosphere, and Climate (COSMIC) which started in late 2006. The temperature
 95 profiles were retrieved by the University Corporation for Atmospheric Research (UCAR)
 96 from 2007 to 2013. We use only dry retrievals over this period which are of the highest
 97 quality in regions with low water vapor concentration such as the tropopause layers [e.g.
 98 *Wickert et al.*, 2005].

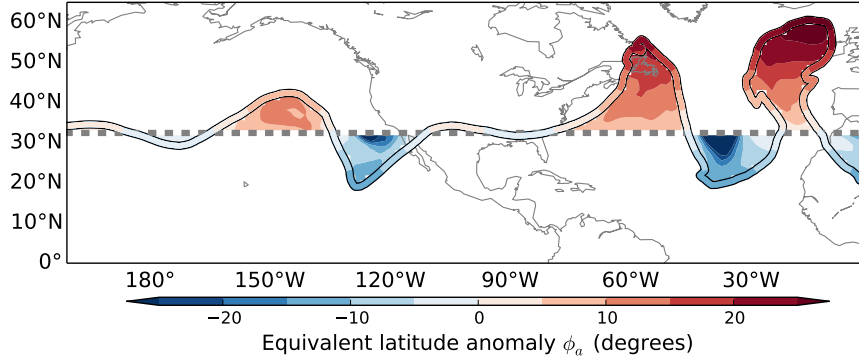
99 To study the spatial pattern of double tropopauses and their corresponding strati-
 100 fication, we transform thousands of temperature profiles over the entire globe each day
 101 into regularly gridded data with a horizontal resolution of $2.5^\circ \times 2.5^\circ$ and vertical resolu-
 102 tion of 500m by linear barycentric interpolation. Such a horizontal resolution is chosen
 103 as a balance between the need for relative fine structure and a limited number of pro-
 104 files. From these gridded daily temperature profiles, we calculate the potential tempera-
 105 ture θ , the Brunt-Väisälä frequency $N^2 = g\partial(\ln\theta)/\partial z$, and the height of the tropopauses
 106 using the definition of the *World Meteorological Organization* [1957]. Specifically, the
 107 first tropopause is defined as the lowest level at which the lapse rate decreases to $2K/km$,
 108 provided that the average lapse rate between this level and any level above within $2km$
 109 is not greater than $2K/km$. Above the first tropopause, if the average lapse rate between
 110 any level and all higher levels within $1km$ exceeds $3K/km$ again, a second tropopause is
 111 defined using the same criteria as the first.

112 **2.2 Reanalysis data**

113 To characterize the dynamical features of double tropopauses, we use potential vor-
 114 ticity (PV) from ERA-Interim reanalysis data [*Dee et al.*, 2011] over the period from Jan-
 115 uary 2007 to December 2013. The PV field has a horizontal resolution of $1.5^\circ \times 1.5^\circ$ and
 116 15 vertical isentropic levels ranging from 265K to 850K. We apply two diagnostics to the
 117 isentropic PV field, which are described in the following subsections.

118 **2.2.1 Equivalent latitude anomaly**

119 Since PV contours on isentropic surfaces are material lines for adiabatic motion in
 120 the absence of friction, PV is an ideal field for characterizing advection by synoptic distur-
 121 bances. Inspired by *Pan et al.* [2009], we first map PV (q) at each grid point to its corre-



133 **Figure 2.** Potential vorticity of 3 PVU (solid contour) on 350K isentropic surface and its corresponding
 134 equivalent latitude ϕ_e (dashed line). The equivalent latitude anomaly ϕ_a (color shading) between the 3 PVU
 135 contour and the equivalent latitude ϕ_e is also plotted.

122 sponding equivalent latitude (ϕ_e) value according to *Butchart and Remsberg* [1986]:

$$\phi_e [q(\lambda, \phi), \theta] = \arcsin \left[1 - \frac{A(q, \theta)}{2\pi a^2} \right] \quad (1)$$

123 where $A(q, \theta)$ is the area enclosed by a q contour on an isentrope θ and a is the radius of
 124 the earth. By this definition, $\phi_e(q, \theta)$ represent the latitude circle that encloses the same
 125 area as the q contour. Figure 2 shows the $q=3$ PVU contour on the 350K isentrope and its
 126 equivalent latitude ϕ_e (dashed line). As shown in Fig. 2, an air parcel's equivalent latitude
 127 can be thought of as the latitude it comes from. Accordingly, the difference between an air
 128 parcel's actual latitude and its equivalent latitude:

$$\phi_a(\lambda, \phi, \theta) = \phi - \phi_e(\lambda, \phi, \theta) \quad (2)$$

129 can be used to measure the meridional excursion experienced by an air parcel due to syn-
 130 optically adiabatic disturbances. Figure 2 illustrates the ϕ_a (shading) enclosed by wave lobes
 131 associated with the $q=3$ PVU contour. Positive ϕ_a (red shading) represents poleward ad-
 132 vection, whereas negative ϕ_a (blue shading) represents equatorward advection.

136 2.2.2 Rossby wave breaking detection

137 As shown in Fig. 2, PV contours are good at depicting the morphology of large-
 138 scale Rossby waves. In particular, wave breaking is featured in Fig. 2 by the horizontal
 139 overturning of the PV contour over the central and eastern North Atlantic. To study these
 140 breaking events and their connections to double tropopauses, we apply the PV-based wave

141 breaking detection algorithm described in *Liu et al.* [2014]. The algorithm detects wave
 142 breaking by searching for overturning of circumpolar 2 PVU contours on isentropic sur-
 143 faces ranging from 300K to 350K with an interval of 5K. According to the direction of
 144 overturning, wave breaking is classified into anticyclonic wave breaking and cyclonic wave
 145 breaking. For example, the overturning in Fig. 2 between 30°W to 20°W is cyclonic,
 146 whereas the overturning between 20°W to 0°W is anticyclonic. For both anticyclonic and
 147 cyclonic wave breaking events, the centroids of the overturning anticyclonic lobes are as-
 148 signed as their centers. Throughout this paper, all composites with respect to wave break-
 149 ing are translated so that the wave breaking centers overlap with each other. For more de-
 150 tails, we refer readers to *Liu et al.* [2014].

151 **2.3 Baroclinic eddy lifecycle simulations**

152 One of the goals of this study is to quantify how much the occurrence of double
 153 tropopauses enhances stratosphere-troposphere exchange compared to situations without a
 154 double tropopause. To serve this goal, we construct a control eddy lifecycle simulation
 155 with no double tropopause and a series of contrasting lifecycle simulations with vary-
 156 ing areal coverage of double tropopauses following *Wang and Polvani* [2011] (hereafter
 157 WP11). The advantage of these simulations is that the only difference among them is
 158 the tropopause structure so that we can cleanly isolate any enhancement of stratosphere-
 159 troposphere exchange due to the occurrence of double tropopauses. Note that we use a
 160 different model from WP11, the Geophysical Fluid Dynamics Laboratory (GFDL) spec-
 161 tral dry dynamical core with a horizontal resolution of T85, and 60 uneven sigma levels.
 162 The initial conditions for the simulations are described in Section 2.3.1, and the setup for
 163 passive tracers is discussed in Section 2.3.2.

164 **2.3.1 Initial conditions**

165 We prescribe baroclinically unstable initial conditions largely following WP11, with
 166 some minor modifications due to the fact that we use a different model. We describe the
 167 procedure briefly here with a focus on the differences from WP11. For the omitted details
 168 that are common to WP11, we refer readers to the Appendices in their paper.

169 As in WP11, the temperature field is determined by the lapse rate field $\Gamma(\phi, z)$ which
 170 blends a low-latitude tropical profile $\Gamma^L(z)$ with a high-latitude one $\Gamma^H(z)$. Both profiles

171 carry a parameter that determines the strength of the TIL: c_L and c_H respectively. The
 172 blending in the meridional direction takes the form:

$$\Gamma(\phi, z) = \Gamma^L(z) + (\Gamma^H(z) - \Gamma^L(z)) \left[\frac{1}{2} + \frac{1}{2} \tanh\left(\frac{\phi - \phi_0}{\phi_D}\right) \right] \quad (3)$$

173 which is almost the same as WP11 except that we replace metric distances Y , Y_0 , and Y_D
 174 with latitudes ϕ , ϕ_0 , ϕ_D , and set $\phi_0 = 45^\circ$, $\phi_D = 10^\circ$. The initial temperature field (T)
 175 is then obtained by integrating the lapse rate from the top of the atmosphere where $T =$
 176 $220K$.

177 With the initial temperature field defined, the zonal wind (U) can be obtained by
 178 utilizing the thermal wind balance on a sphere:

$$-\frac{R}{H} \frac{\partial T}{\partial \phi} = (af + 2U \tan \phi) \frac{\partial U}{\partial z} \quad (4)$$

179 where R is the ideal gas constant, H is the scale height, and a is the radius of the earth.
 180 This differs from the thermal wind balance in WP11 where an f-plane model was used.
 181 The zonal wind can be solved for by iterating the vertical integration of (4) as:

$$U^{i+1}(\phi, z) = \int_0^z -\frac{R}{H (af + 2U^i(\phi, z^*) \tan \phi)} \frac{\partial T}{\partial \phi} dz^* \quad (5)$$

182 where we set $U(\phi, 0) = 0$. With an initial guess of $U^0(\phi, z) = 0$, the U^i converges very
 183 quickly for the initial temperature field employed here (within a few iterations).

184 WP11 was able to increase the area of double tropopauses by increasing the strength
 185 of the initial high-latitude TIL strength c_H . The reason why a strong high-latitude TIL
 186 helps form double tropopause is one subject of this study and will be revisited in Section
 187 4.2. To increase the coverage of double tropopauses, we follow WP11 except that we in-
 188 crease the strength of the low-latitude TIL c_L by the same amount, so that the resulting
 189 jet streams have nearly the same strength under both the weak and strong TIL cases. We
 190 carry out five simulations with c_H values ranging from $0K/km$ to $4K/km$ with an inter-
 191 val of $1K/km$. For the low-latitude TIL strength, we always set it as $c_L = c_H + 3K/km$.
 192 The specific difference $3K/km$ is chosen to result in reasonable initial jets with a max-
 193 imum zonal wind of approximately $50m/s$ throughout all of the five simulations. These
 194 five simulations are referred to by the high-latitude TIL strength (TIL0 through TIL4). To
 195 study the mechanisms of double tropopause formation, two of these simulations – TIL0
 196 and TIL3 – are also used in Section 4.2.

197

2.3.2 Tracer setup

To quantify the influence of double tropopauses on stratosphere-troposphere exchange, we initialize two passive tracers S and T following *Polvani and Esler* [2007]. In particular, we pick the $N_{tp}^2 \equiv 3.5 \times 10^{-4} s^{-2}$ contour as the initial tropopause. We then initialize the two tracers on isentropes ranging from 290K to 500K as:

$$S = \mathcal{H}(N^2 - N_{tp}^2) \quad (6a)$$

$$T = \mathcal{H}(N_{tp}^2 - N^2) \quad (6b)$$

where $\mathcal{H}()$ is the Heaviside function:

$$\begin{cases} \mathcal{H}(x) = 1, & x \geq 0 \\ \mathcal{H}(x) = 0, & x < 0 \end{cases}$$

$S + T = 1$ at all times by construction. After $t = 0$ we use the contour of $S = T = 0.5$ as the natural tropopause. The mass of S in the troposphere is viewed as the accumulated stratosphere-to-troposphere (*STT*) tracer mass flux and the mass of T in the stratosphere is viewed as the accumulated troposphere-to-stratosphere (*TTS*) tracer mass flux:

$$STT = \oint \mathcal{H}(T - 0.5) S \rho dV \quad (7a)$$

$$TTS = \oint \mathcal{H}(S - 0.5) T \rho dV \quad (7b)$$

198

3 The synoptic features of double tropopauses

199

200

201

202

203

204

205

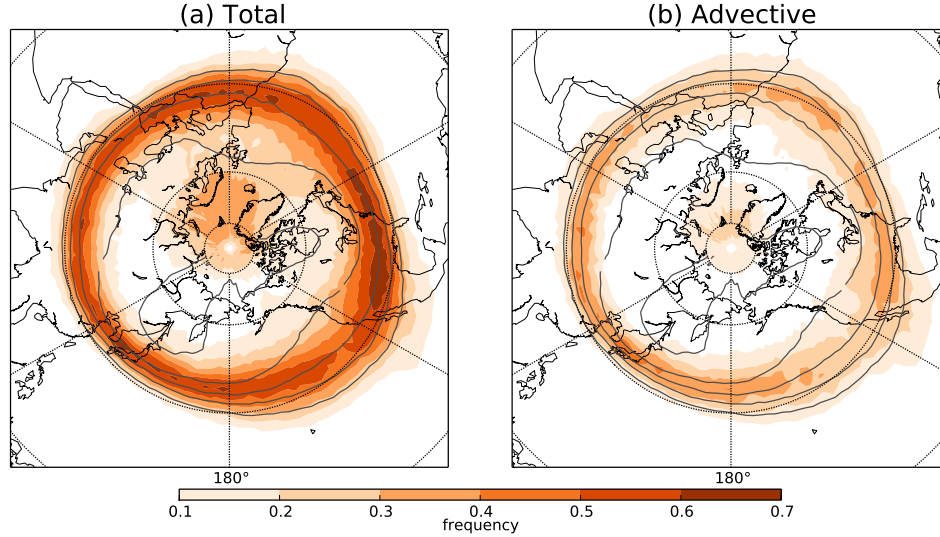
206

207

208

209

Although conforming to the same WMO definition, the actual vertical temperature profiles of double tropopauses can vary substantially. Figure 1 exemplifies two types of double tropopause profiles from the COSMIC GPS data. In Fig. 1a, both the first and the second tropopauses mark a discontinuity in the thermal stratification in a similar way. Between the two tropopauses, there is a layer (13-16km in altitude) with a tropospheric lapse rate of $5 - 6K/km$, similar to the lapse rate below the first tropopause. In some ways, the stratification around the second tropopause looks like a replication of that around the first tropopause. This suggests that the second tropopause in Fig. 1a may have existed before and the double tropopause was formed by horizontal advection. In Fig. 1b, the second tropopause does not mark a discontinuity, but a threshold defined by the WMO as the lapse rate decreases gradually with height back below $2K/km$. In this case, the second

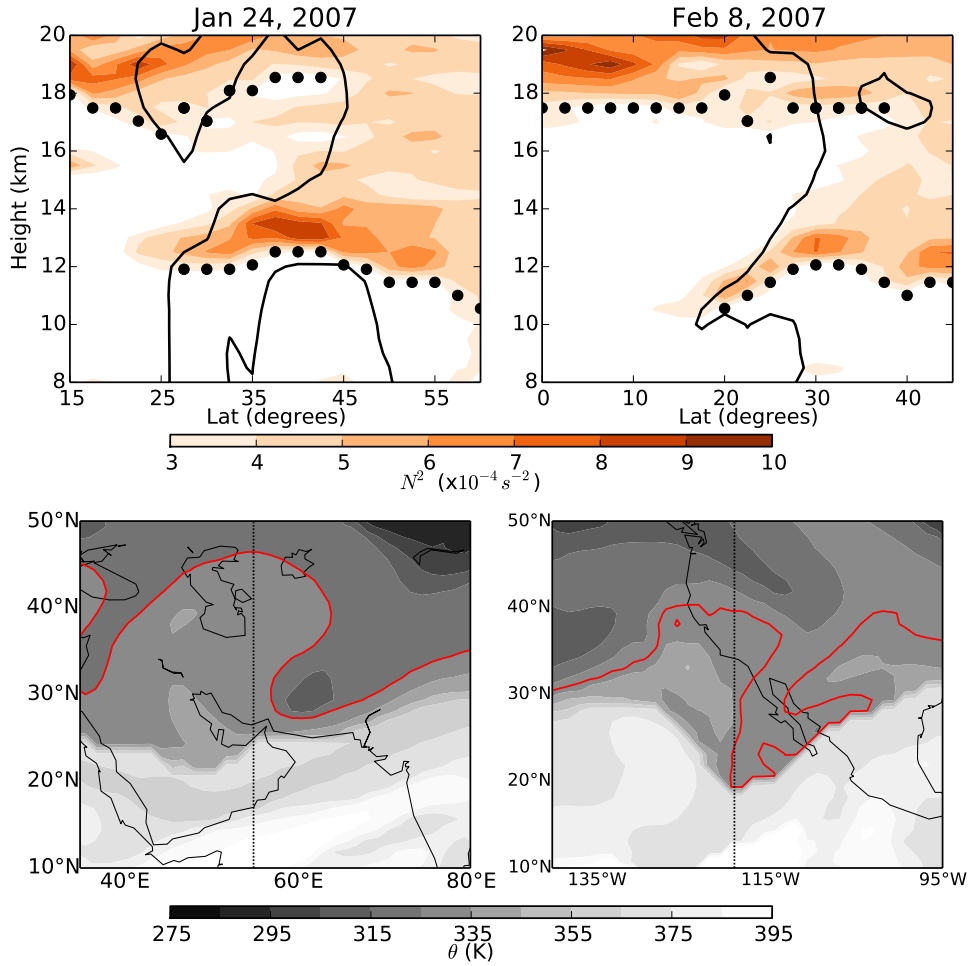


213 **Figure 3.** Climatology of double tropopause frequency (shading) in the Northern Hemisphere during win-
 214 ter for (a) total occurrence, and (b) occurrence due to differential advection (see Section 4.1 for details). Grey
 215 contours denote the climatological height of the first tropopause with an interval of 1.5km, with the largest
 216 being 15.5km.

210 tropopause seems more likely to have been created by local changes in the thermal strat-
 211 ification. In this section, we focus on the general features of double tropopauses first and
 212 address two possible formation mechanisms in Section 4.

217 Using COSMIC GPS data, the wintertime climatology of double tropopauses oc-
 218 currence from 2007 to 2013 is shown in Fig. 3a (shading) along with the corresponding
 219 height of the first tropopause (contour). The double tropopauses generally occur in the
 220 subtropics within the 30°N to 40°N band where the climatological tropopause slope is
 221 most steep (grey contours). Their most frequent occurrence is located over North Amer-
 222 ica and the northwest Atlantic, which is consistent with *Randel et al.* [2007a]. Away from
 223 the subtropics, double tropopauses also occur at higher latitudes over the North Atlantic,
 224 maximizing near the Norwegian Sea and the Greenland Sea.

232 To illustrate the synoptic features associated with double tropopauses, we show snap-
 233 shots of two individual events in the two columns of Fig. 4. The upper row shows the
 234 meridional cross sections of thermal stratification N^2 (shading) and the equivalent latitude
 235 contour of $\phi_e = 30^\circ N$ derived from PV. The black dots denote the tropopauses identified
 236 by the WMO definition. The lower row shows potential temperature on the 2PVU sur-



225 **Figure 4.** The left column shows an event on Jan 24, 2017 and the right column shows an event on Feb 8,
 226 2017. **Upper row:** Snapshots of the Brunt-Väisälä frequency N^2 (shading) from GPS temperature data and
 227 equivalent latitude contour $\phi_e = 30^\circ$ (black contour) from ERA-Interim reanalysis. The black solid circles
 228 denote the tropopause identified by GPS temperature data. **Lower row:** Potential temperature θ (grey shad-
 229 ing, unit: K) on the 2 PVU surface which represents the dynamical tropopause. The dotted lines denote the
 230 longitude at which those cross sections are taken and shown in the upper row. The red contours accent the
 231 overturning of θ .

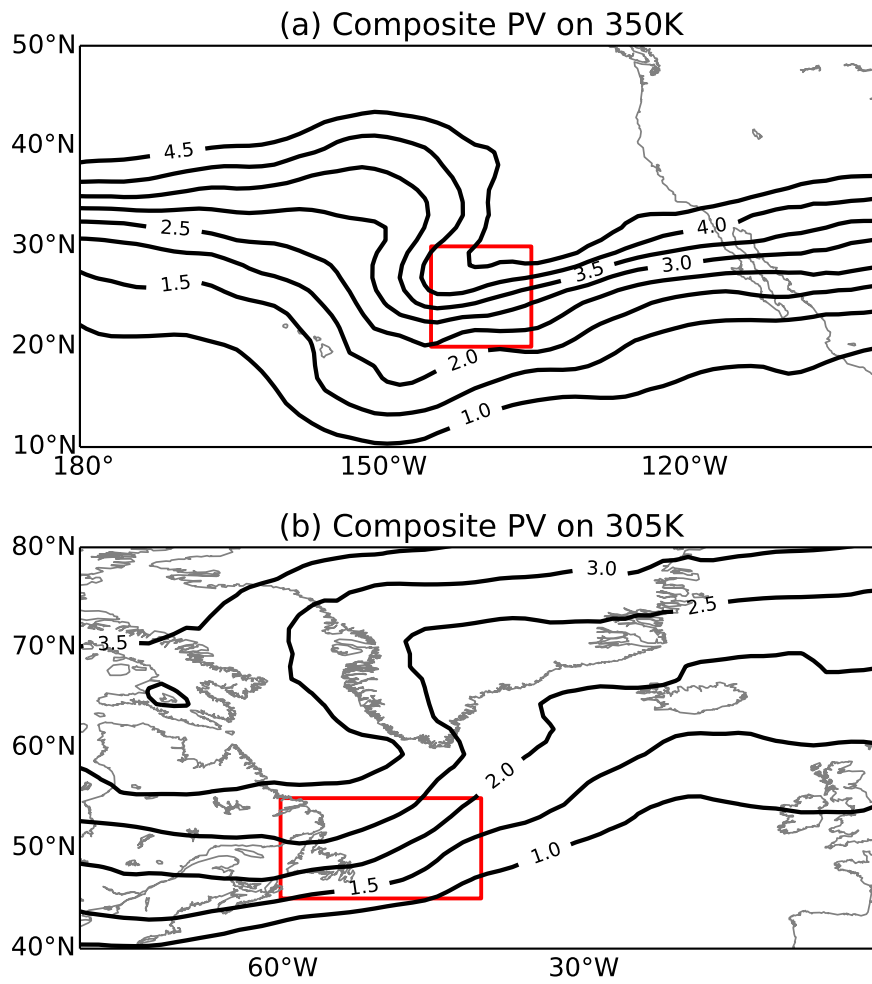
237 face, representing the dynamical tropopause. For the event on Jan 24 (left column of Fig.
 238 4), the stacking of two tropopauses occurs between 25°N to 45°N , with the tropopauses
 239 vertically separated by a distance of about 6km. Corresponding to this tropopause struc-
 240 ture, the N^2 field exhibits a clockwise folding. The cause of this folding is revealed by the
 241 $\phi_e = 30^\circ\text{N}$ contour, which reaches 45°N at the higher tropopause level. Assuming the air

242 on the contour is from 30°N, this indicates a substantial poleward advection of the higher
 243 tropopause which then overlapped with the extratropical lower tropopause that remained
 244 relatively stationary. In the lower panel of Fig. 4, we show that the strong poleward intru-
 245 sion at the higher tropopause level happened as a result of horizontal overturning corre-
 246 sponding to an anticyclonic wave breaking event.

247 The event on Feb 8 makes an interesting comparison with the event on Jan 24 and
 248 is shown in the right column of Fig. 4. The vertically stacked tropopauses are separated
 249 by 5-7km and a clockwise folding of N^2 contour is also seen. As in the previous case, the
 250 shape of the $\phi_e = 30^\circ N$ contour aligns well with the N^2 contour, indicating that differen-
 251 tial advection caused the folding of the $\phi_e = 30^\circ N$ contour. However, the difference is that
 252 this event was dominated by an equatorward intrusion, rather than a poleward intrusion.
 253 Specifically, the air at the lower tropopause level was advected from 30°N equatorward to
 254 20°N while the air at the higher tropopause barely moved from its equivalent latitude. The
 255 result is that the lower extratropical tropopause moved equatorward and overlapped with
 256 the tropical tropopause above. Examining the horizontal advection pattern (lower panel of
 257 Fig. 4), we also find an anticyclonic wave breaking event providing the critical equator-
 258 ward intrusion. But the intrusion was associated with breaking wave's equatorward lobe,
 259 rather than the poleward lobe.

262 The two examples above suggest a possible link between Rossby wave breaking and
 263 double tropopauses. We further support this linkage by compositing PV with respect to
 264 the occurrence of double tropopauses in specific regions (Fig. 5). Specifically, PV is com-
 265 posited for days when more than 80% of the GPS temperature profiles within the red rect-
 266 angle exhibit double tropopauses. Both composites in Fig. 5 exhibit large-scale horizontal
 267 overturning of PV contours indicative of Rossby wave breaking. In particular, the dou-
 268 ble tropopauses over the subtropical northeastern Pacific tend to occur in the equatorward
 269 lobe of anticyclonic wave breaking (Fig. 5a), whereas those over the Labrador Sea tend to
 270 occur in the equatorward lobe of a cyclonic wave breaking (Fig. 5b).

271 As Rossby wave breaking is shown to be linked to double tropopauses climatolog-
 272 ically, we ask “what are the mechanisms through which they are linked”. The snapshots
 273 in Fig. 4 suggest that wave breaking may help form double tropopauses by providing
 274 vertically differential advection, either stronger poleward advection of the higher tropical



260 **Figure 5.** Composite potential vorticity (PV) in unit of PVU on isentropes for days when more than 80% of
261 profiles within the red rectangle exhibit double tropopauses.

275 tropopause or stronger equatorward advection of the lower extratropical tropopause. We
 276 will further investigate this hypothesis in the next section.

277 **4 Mechanisms for the adiabatic formation of double tropopauses**

278 Since double tropopauses are defined by thermal stratification, looking at its bud-
 279 get should provide clues to the formation of double tropopauses. Below is the adiabatic
 280 prognostic equation of N^2 using the approximation of thermal wind balance for large-scale
 281 flow:

$$\frac{\partial N^2}{\partial t} = \underbrace{-\mathbf{V} \cdot \nabla N^2}_A + N^2 \underbrace{\frac{\partial w}{\partial z}}_B \quad (8)$$

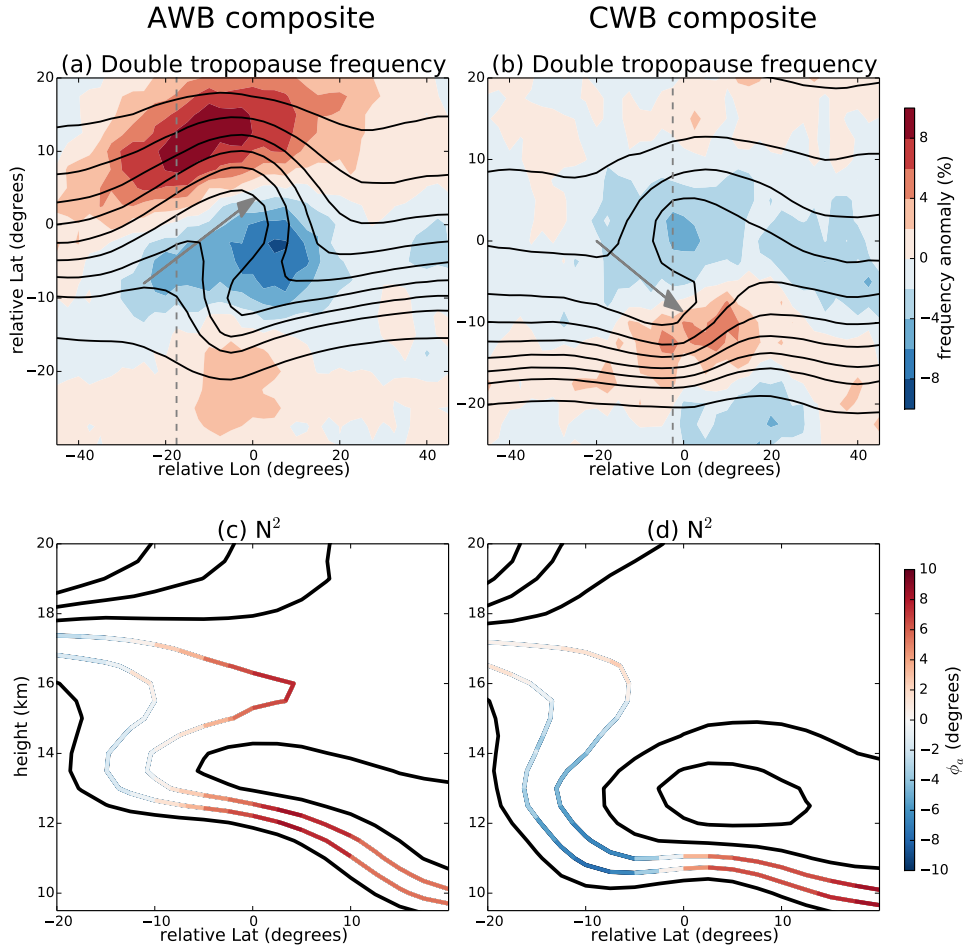
282 The terms on the RHS correspond to two physical processes that contribute to the local
 283 change in N^2 , as alluded to in Fig. 1. The first is the advection term (A) and the other is
 284 the compression/stretching term (B) that produces/destroys N^2 . When the production term
 285 B is small, N^2 behaves like a passive tracer and the formation of double tropopause can
 286 be mainly attributed to differential horizontal advection. When the production term is not
 287 small, double tropopauses can be formed even in the absence of differential advection. We
 288 explore these two mechanisms in the next two subsections.

289 While the evolution of N^2 is likely always a mixture of both A and B, we aim to
 290 understand the behavior of tropopause evolution under each separately as a stepping stone
 291 to understanding more complex scenarios. In addition, we illustrate in observations and
 292 model simulations that the formation of double tropopause can at times be predominantly
 293 determined by one of these two mechanisms.

294 **4.1 Differential advection**

295 Snapshots in Fig. 4 illustrate a possible mechanism by which Rossby wave breaking
 296 helps form double tropopauses – providing differential advection. To examine how ro-
 297 bust this mechanism is in climatology, we composite variables for the two types of Rossby
 298 wave breaking events in Fig. 6. The upper row shows the composite double tropopause
 299 frequency anomaly relative to the local climatology (shading) and the lower row shows the
 300 the corresponding thermal stratification and advection pattern. The composites are made
 301 by horizontally shifting the fields about the wave breaking centers, so the x and y axes are
 302 relative longitude and latitude respectively. We only use centers with a latitude between

303 30°N and 55°N, to focus on the region where the climatological tropopause is steep and
 304 differential advection is most likely to operate.



305 **Figure 6.** Composite variables for anticyclonic wave breaking (AWB) in the left column and cyclonic wave
 306 breaking (CWB) in the right column. The fields are moved horizontally so that the centers for each type of
 307 wave breaking overlap. The longitude and latitude shown on axes are relative to the wave breaking centers.
 308 **Upper row:** Anomalous frequency of double tropopause occurrence (shading) and potential temperature θ
 309 (contour) on the 2 PVU surface which represents the dynamical tropopause. **Lower row:** Cross section of N^2
 310 (contour) taken along the dashed lines in the upper row. The color shading is added to the folding contours
 311 and denotes the equivalent latitude anomaly ϕ_a . The interval of the N^2 contours is $0.5 \times 10^{-4} s^{-2}$, and the
 312 value for the two colored contours are $3.5 \times 10^{-4} s^{-2}$, $4 \times 10^{-4} s^{-2}$ respectively.

313 Double tropopauses occur significantly more frequently than climatology to the
 314 north of anticyclonic wave breaking (Fig. 6a). Higher frequencies of double tropopauses

315 also occur to the south of anticyclonic wave breaking's equatorward lobe, but with much
 316 weaker strength. To visualize the vertical structure of stratification associated with the
 317 anomalous double tropopause formation shown in Fig. 6a, we plot a meridional cross sec-
 318 tion of N^2 (contours) along -17.5° relative longitude in Fig. 6c. The N^2 contours folds
 319 substantially in the composite, demonstrating the robustness of this double tropopause
 320 structure. To see if the folding is related to differential advection, we color the folding
 321 contours by their anomalous equivalent latitude ϕ_a . The red shading indicates poleward
 322 advection and the blue shading indicates equatorward advection. The folding in Fig. 6c is
 323 mainly associated with extensive poleward advection at 16km height and little advection
 324 near 13.5km, depicting a major role for differential advection in the formation of these
 325 double tropopauses in a composite sense. Comparing Fig. 6a and Fig. 6c, one can see the
 326 poleward advection north of -10° relative latitude is provided by the poleward advection of
 327 anticyclonic wave breaking, as is also exemplified in the left column of Fig. 4.

328 For cyclonic wave breaking, the largest positive anomaly of double tropopause fre-
 329 quency occurs at the south edge of its equatorward lobe (Fig. 6b). To visualize the merid-
 330 ional structure of thermal stratification associated with the largest anomaly, another cross
 331 section is taken along -2.5° relative longitude and shown in Fig. 6d. Similar to anticy-
 332 clonic wave breaking, N^2 contours fold substantially, indicating the robustness of the dou-
 333 ble tropopause anomalies. What is different, however, is that the folding is dominated by
 334 equatorward advection of the lower tropopause near the height of 11km. The dominating
 335 equatorward advection to the south of -5° relative latitude is provided by the equatorward
 336 lobe of cyclonic wave breaking. Comparing Fig. 6c with Fig. 6d, it is evident that the
 337 double tropopauses formed in the cyclonic lobe by equatorward advection are more verti-
 338 cally separated than those formed in the anticyclonic lobe by poleward advection, which
 339 is also alluded in Figs. 4a and 4b. This is consistent with *Wirth* [2001] who studied the
 340 double tropopauses resulting from idealized differential advection of PV.

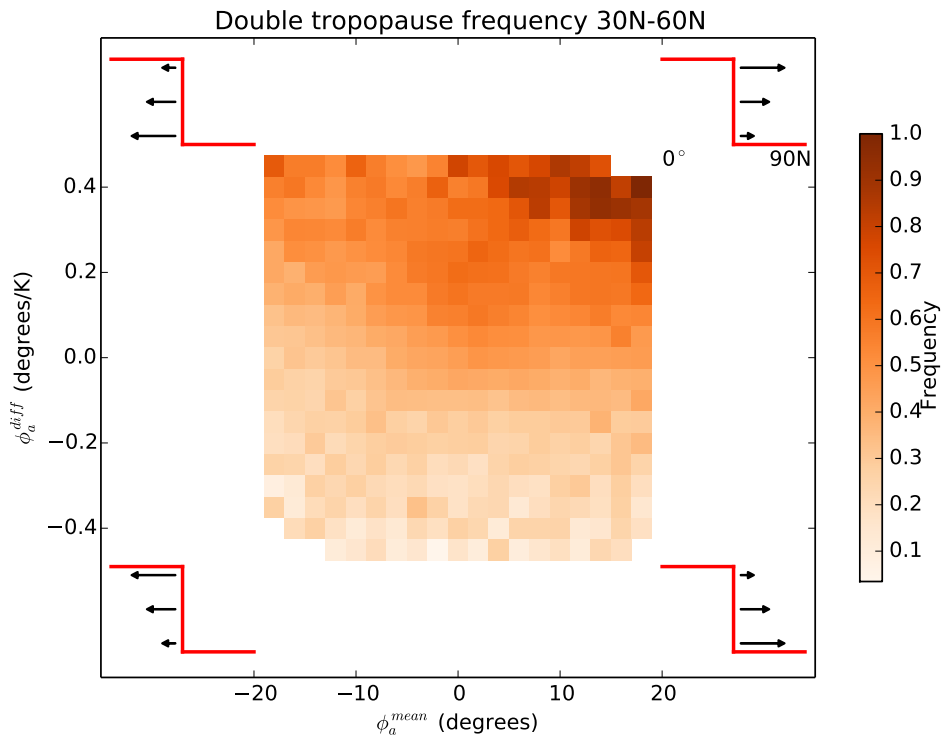
341 The composites for wave breaking along with snapshots in Fig. 4 demonstrate that
 342 differential advection can dominate the formation of double tropopauses in a composite
 343 sense. We proceed by addressing how often this happens, regardless of the occurrence of
 344 wave breaking. To answer this, we classify each double tropopause occurrence into ad-
 345 vective and non-advective using the equivalent latitude ϕ_e field. In words, for each sec-
 346 ond tropopause, we test if it still overlaps with a lower tropopause after we move all the

347 tropopauses meridionally to their equivalent latitudes. If it does, we classify it as a non-
 348 advective double tropopause. Otherwise we mark it as advective.

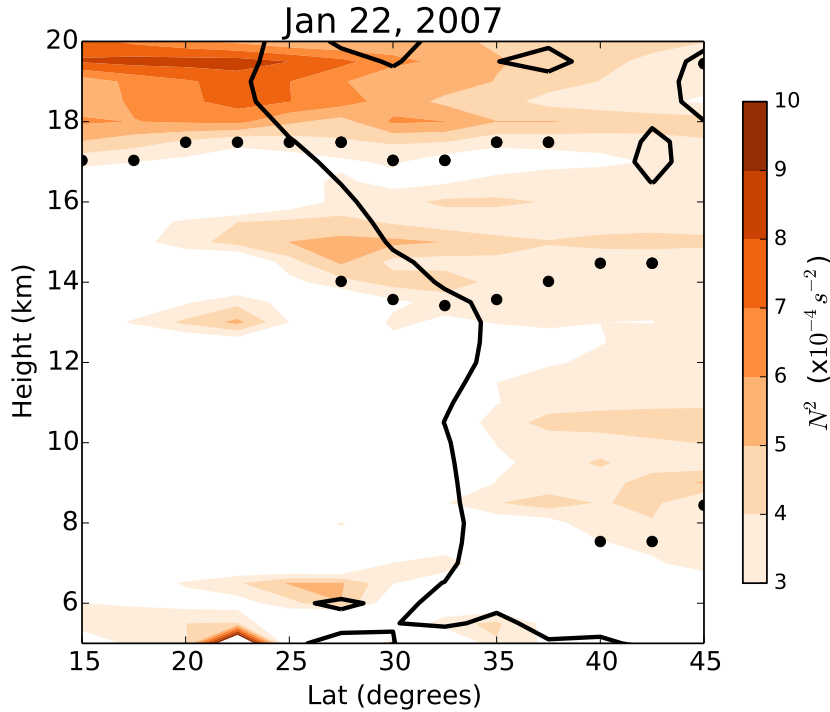
349 The result of the classification is shown in Fig. 3b. Advective double tropopause
 350 occurrence is more confined in the tropopause break region than the total occurrence.
 351 This supports the hypothesis that the advective mechanism is most likely to operate in the
 352 tropopause break region. In particular, the most frequent occurrence of advective double
 353 tropopauses is located over east Asia and the North Pacific near Japan where the tropopause
 354 slope is steepest. Summing up the total occurrence of advective double tropopauses, dif-
 355 ferential advection appears to account for 47% of the total occurrence of double tropopauses
 356 in the Northern Hemisphere.

357 Besides differential advection, previous studies have also focused on the direction
 358 of the mean advection above the first tropopause [e.g. *Pan et al.*, 2009; *Añel et al.*, 2012;
 359 *Schwartz et al.*, 2015; *Wang and Polvani*, 2011]. We next quantify how favorable various
 360 advection patterns are for double tropopause formation. Specifically, we take all the GPS
 361 profiles and calculate the frequency of double tropopause as a function of both mean ad-
 362 vection (ϕ_a^{mean}) and differential advection (ϕ_a^{diff}) associated with the profiles (Fig. 7).
 363 Positive and negative ϕ_a^{mean} indicates poleward and equatorward mean advection respec-
 364 tively. Positive and negative ϕ_a^{diff} indicate clockwise and counterclockwise folding re-
 365 spectively. The four corners of Fig. 7 correspond to the four combined advection patterns
 366 which are illustrated by schematics at their corresponding corners. For detailed definitions
 367 of ϕ_a^{mean} and ϕ_a^{diff} , we refer readers to Appendix A.

373 In Fig. 7, the occurrence of double tropopauses is largely dictated by differential
 374 advection ϕ_a^{diff} . That is, the frequency of double tropopauses is mainly stratified in the
 375 vertical direction of the plot, becoming increasingly more frequent as the value of ϕ_a^{diff}
 376 increases for any ϕ_a^{mean} bin. Particularly large increases occur near the transition from
 377 negative ϕ_a^{diff} to positive ϕ_a^{diff} , the latter of which represents the favorable shear di-
 378 rection for forming double tropopauses. When the shear direction is in favor of double
 379 tropopauses ($\phi_a^{diff} > 0$), poleward mean advection ($\phi_a^{mean} > 0$) is more likely to form
 380 double tropopauses than equatorward mean advection ($\phi_a^{mean} < 0$). Physically, this means
 381 that double tropopauses are more likely to be formed by the poleward advection of the
 382 higher tropopause than the equatorward advection of the lower tropopause. This is consis-
 383 tent with *Castanheira and Gimeno* [2011] where they found the poleward edge of double



368 **Figure 7.** The frequency of wintertime double tropopauses for COSMIC GPS profiles binned by mean
 369 equivalent latitude anomaly ϕ_a^{mean} (x-axis) and the vertical shear of equivalent latitude anomaly ϕ_a^{diff}
 370 (y-axis). ϕ_a^{mean} and ϕ_a^{diff} are calculated from ERA-Interim reanalysis. The meridional advection patterns
 371 corresponding to the four corners are illustrated by schematics, with red lines denoting the tropopauses and
 372 black arrow denoting the meridional wind.



391 **Figure 8.** Snapshots of the Brunt-Väisälä frequency N^2 (shading) from GPS temperature data and equiva-
 392 lent latitude contour $\phi_e=35^\circ$ (black contour) from ERA-Interim reanalysis on Jan 22, 2007. The black solid
 393 circles denote the tropopause identified by GPS temperature data.

384 tropopause area is better correlated with the meridional extent of double tropopauses than
 385 the equatorward edge. The preferred poleward advection of tropospheric air is also sug-
 386 gested by *Castanheira et al.* [2012] where lower total column ozone is found for double
 387 tropopauses. Since ozone is rich in the stratosphere, lower column ozone indicates more
 388 tropospheric air in the column and hence suggests a poleward tropospheric intrusion into
 389 the stratosphere.

390 4.2 Destabilization/vertical stretching

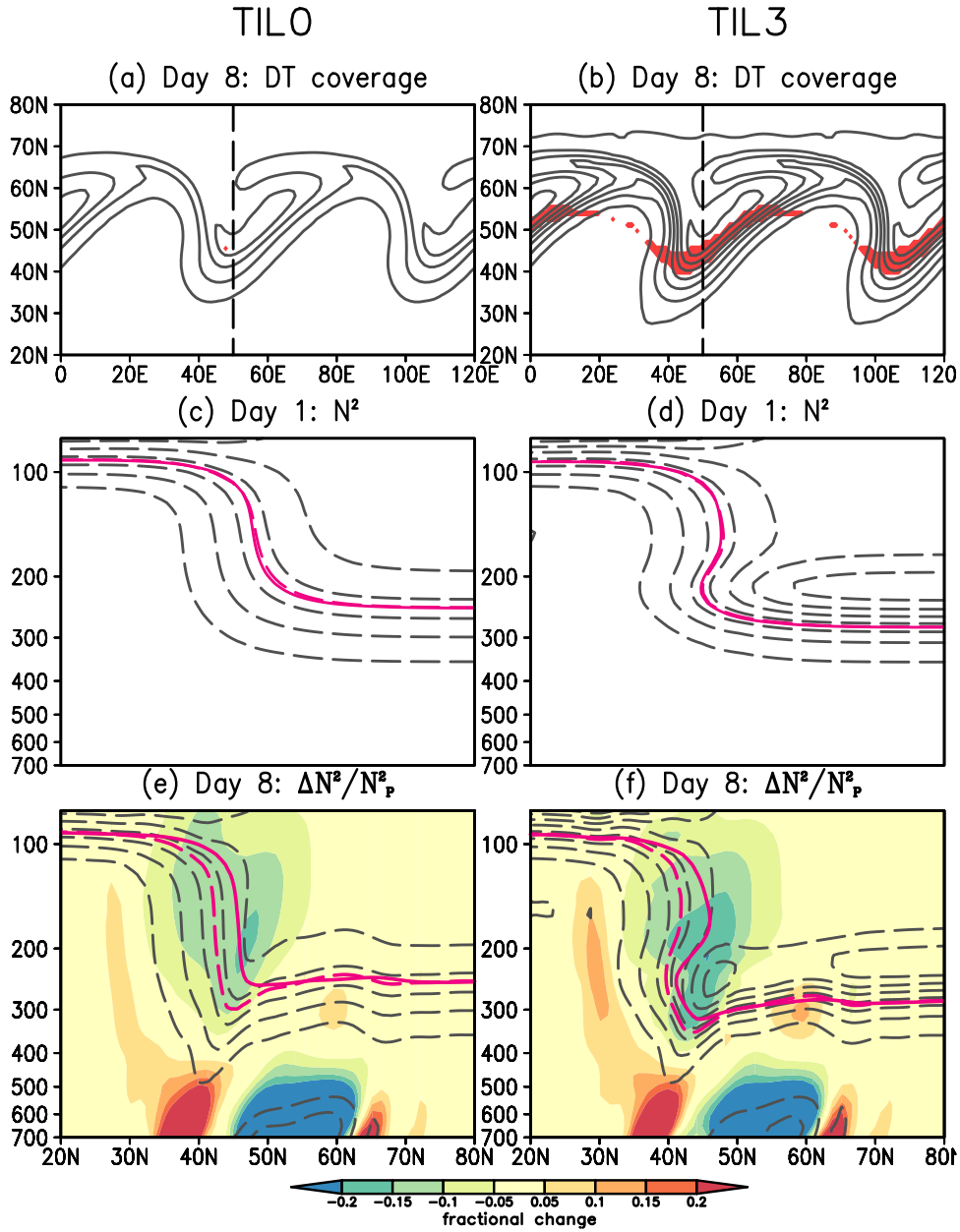
394 In the previous section we showed that approximately half of double tropopauses are
 395 formed directly by differential advection. In this section we explore possible mechanisms
 396 for the formation of the other 50%. Figure 8 shows a cross section of a double tropopause
 397 event that is not directly caused by differential advection. The stacking of tropopauses oc-
 398 curs between 27°N and 38°N where the N^2 field (shading) shows a clockwise folding.

399 However, the equivalent latitude (ϕ_e) contour of 30°N (contour) shows a counterclock-
 400 wise folding. This contrasts with the cases shown in Figs. 4 where the ϕ_e contour ap-
 401 proximately aligned with the N^2 contours, indicating that N^2 behaved largely as a pas-
 402 sive tracer. In Fig. 8, the non-passive behavior of N^2 indicates that production/destruction
 403 processes of thermal stratification might be responsible for this double tropopause event,
 404 such as the vertical stretching term B of (8).

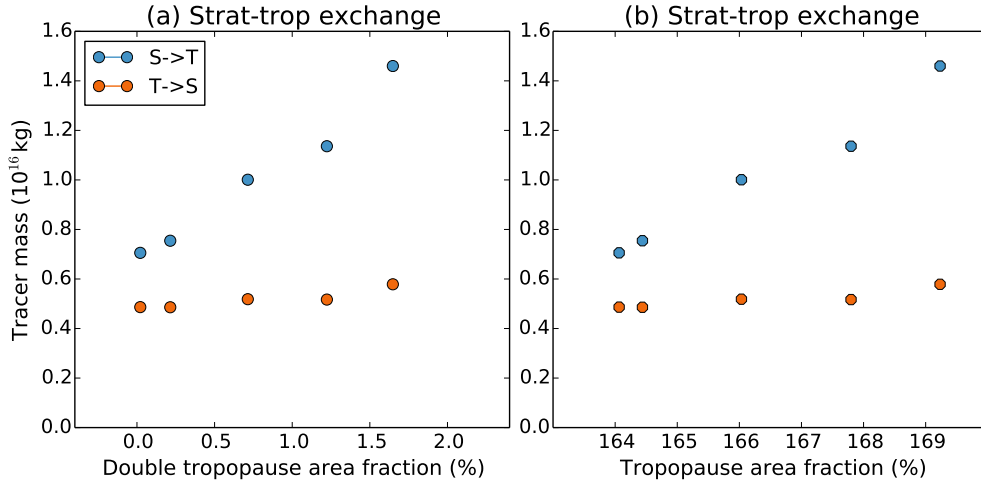
405 Since stretching/compression is the only destruction/production process for adiabatic
 406 N^2 , we quantify the accumulated effect of this stretching/compressing process by compar-
 407 ing N^2 with its passive counterpart in adiabatic situations. In particular, we conduct adia-
 408 batic eddy lifecycle simulations as described in Section 2.3 and initialize a passive tracer
 409 N_P^2 that has the same initial value as N^2 . Then the difference $\Delta N^2 = N^2 - N_P^2$ quantifies
 410 the accumulated destruction/production of N^2 , namely the effect of stretching/compression
 411 that destabilizes/stabilizes the thermal stratification. We further normalize ΔN^2 by N^2 to
 412 get the fractional change of N^2 due to stretching/compression.

419 The quantification of destabilization/stabilization and its role in forming double
 420 tropopause during the eddy lifecycle simulations is summarized in Fig. 9. The left col-
 421 umn shows a simulation with no TIL (hereafter TIL0) and the right column shows a sim-
 422 ulation with a TIL of strength $c_H = 3\text{K}/\text{km}$ (hereafter TIL3). The upper row shows that
 423 TIL3 has double tropopause in the cyclonic lobe of wave breaking (red shading) whereas
 424 TIL0 does not. Note that the identification of double tropopause is the same as in WP11,
 425 replacing the 3K/km criteria in the WMO by 2K/km. Also shown in the upper row is N_P^2
 426 (contour) which depicts the horizontal advection pattern. Despite the difference in double
 427 tropopause coverage between TIL0 and TIL3, there is no obvious reason that this differ-
 428 ence is due to difference in the horizontal advection pattern. This suggests that TIL may
 429 influence the formation of double tropopause through some other mechanisms than hori-
 430 zontal advection.

431 The middle and bottom rows of Fig. 9 show cross sections of N_P^2 (dashed contour)
 432 on day 1 and day 8. The tropopause ($N^2 = 3.3 \times 10^{-4}\text{s}^{-2}$) is highlighted for both N_P^2
 433 (dashed magenta) and N^2 (solid magenta), so that the solid magenta contour denotes the
 434 actual tropopause and the dashed magenta contour denotes the hypothetical tropopause
 435 if there were no stretching/compression. The two tropopause contours are same on day
 436 1 but differ on day 8 in the tropopause break region between 40°N and 50°N . The frac-



413 **Figure 9. Left column:** (a) Concentration of N_p^2 tracer (contour) and the location of double tropopauses
 414 (red shading) in the simulation without an extratropical TIL. (c) Cross section of N_p^2 (dashed contour) and N^2
 415 (solid line) along the dashed line shown in (a) on day 1. The magenta contours have a value of $3.3 \times 10^{-4} \text{ s}^{-2}$
 416 and represents the thermal tropopause. Black contours have an interval of $0.5 \times 10^{-4} \text{ s}^{-2}$. (e) The contours
 417 are the same as in (c) but for day 8. The shading is the fractional material change in thermal stratification
 418 $\Delta N_p^2/N_p^2$. **Right column:** The same as the left column, except for the simulation with an extratropical TIL.



453 **Figure 10.** Accumulated tracer mass flux between the stratosphere (S) and the troposphere (T) in idealized
 454 eddy lifecycle simulations as a function of (a) area fraction of double tropopauses coverage, and (b) area
 455 fraction of the tropopause. The area fraction is a unitless value defined as area divided by the global surface
 456 area.

437 tional stretching/compression ($\Delta N^2/N_p^2$) that leads to such a change is plotted as shading
 438 in the bottom row. In particular, for both TIL0 and TIL3 it is the stretching (blue shading
 439 in Figs. 9e-f) in the tropopause break region that destabilizes the thermal stratification and
 440 hence causes the actual thermal tropopause to deviate from its hypothetical counterpart.
 441 However, the specific deviations are not the same for TIL0 and TIL3, as the former does
 442 not increase tropopause folding whereas the latter does. Interestingly, this is not due to
 443 the stretching (ΔN^2) but the initial N^2 that ΔN^2 adds to. In the case of TIL0, the stretch-
 444 ing/destabilization destroyed the initial tropopause and created a new one above it between
 445 40°N and 50°N, so that the net effect was to move the tropopause upward (Fig. 9e). In
 446 the case of TIL3, while the stretching created a new tropopause at higher levels, it was
 447 not able to destroy the lower initial tropopause because of the strong initial stratification
 448 (N^2) (Figs. 9d and 9f). The result is the stacking of two tropopauses between 40°N and
 449 45°N. Due to these differences in the initial stratification – with or without a TIL – destab-
 450 ilizations of similar strength and spatial pattern lead to very different modification of the
 451 thermal tropopause.

5 Enhancement of stratosphere-troposphere exchange

Both double tropopauses and wave breaking are important processes that enhance the stratosphere-troposphere exchange by disturbing the tropopause interface. While detailed quantification of exchange during idealized wave breaking simulations was performed by *Polvani and Esler* [2007], the impact of double tropopauses on stratosphere-troposphere exchange has not been quantified to the best of our knowledge. Here, we ask to what extent the occurrence of double tropopauses enhances the stratosphere-troposphere exchange during wave breaking events. To answer this question, we use the same setting as in the previous section to generate idealized model simulations with various extents of double tropopauses. In particular, we simulate five eddy lifecycles (TIL0-TIL4) featuring initial TIL strength ranging from $0K/km$ to $4K/km$ (see Section 2.3.1 for details), with TIL0 and TIL3 also being used to study the formation mechanisms of double tropopause in Section 4.2. Then we apply the method of *Polvani and Esler* [2007] to quantify the corresponding strength of the stratosphere-troposphere exchange. In words, we quantify the amount of stratospheric tracer in the troposphere and the amount of tropospheric tracer in the stratosphere as the two-way mass exchange across the tropopause (see 2.3.2 for details). The results are plotted in Fig. 10a as a function of double tropopause area fraction (the coverage area divided by global surface area $4\pi a^2$). As the area fraction of double tropopauses increases, the troposphere-to-stratosphere exchange stays largely unchanged but the stratosphere-to-troposphere exchange increases substantially, as much as double the magnitude when no double tropopause is present.

One way double tropopauses may amplify the stratosphere-to-troposphere exchange during wave breaking is by increasing the area of the tropopause by vertical folding. As the tropopause area increases, there exists a larger interface between the stratosphere and the troposphere for transport and mixing to occur and thus, this might lead to more exchange of air mass. We test this by calculating the total tropopause area (A_{TP}) as the area of the isosurface $S=T=0.5$ during these experiments. We then plot the mass exchange as a function of $A_{TP}/4\pi a^2$ in Fig. 10b. As the tropopause area increases, the troposphere-to-stratosphere exchange stays largely unchanged but the stratosphere-to-troposphere exchange increases significantly, similar to Fig. 10a. This provides evidence that the increase in the tropopause area is the mechanism by which double tropopauses enhance the stratosphere-troposphere exchange. Combining this with the results shown in Fig. 9b, we argue that the

488 increased tropopause area by double tropopauses in wave breaking lobes can substantially
 489 enhance the strength of stratosphere-to-troposphere exchange.

490 **6 Conclusions and discussion**

491 Using COSMIC GPS data, ERA-Interim reanalysis, and eddy lifecycle simulations
 492 of the GFDL dynamical core, we investigate the synoptic features and transport/mixing
 493 strength of double tropopauses, as well as the adiabatic mechanisms responsible for their
 494 formation. In particular, we address three questions with their summarized answers below:

495 1. *What is the relationship between double tropopauses and Rossby wave breaking in the*
 496 *observations?*

497 In a composite sense, anticyclonic and cyclonic wave breaking are both linked to
 498 increased double tropopause occurrence (Fig. 6), and double tropopause occurrence
 499 in certain regions also shows the signature of both types of wave breaking (Fig. 5).

500 2. *What are the mechanisms responsible for double tropopause formation?*

501 We propose two mechanisms. The first one is differential advection of thermal
 502 stratification that leads to the folding of the thermal tropopause (Fig. 4). In particu-
 503 lar, Rossby wave breaking helps form double tropopauses by providing such differ-
 504 ential advection in the observations (Fig. 6). Climatologically, approximately 50%
 505 of all the double tropopauses are formed by this mechanism (Fig. 3). The second
 506 mechanism is the creation of the tropopause by destabilizing the thermal stratifica-
 507 tion in the presence of a TIL (Fig. 9).

508 3. *How do double tropopauses impact stratosphere-troposphere exchange?*

509 In idealized eddy lifecycle simulations, the occurrence of double tropopauses sub-
 510 stantially enhances the stratosphere-to-troposphere exchange (Fig. 10), whereas
 511 the troposphere-to-stratosphere exchange is largely unchanged. We suggest that
 512 the enhancement is due to increased tropopause area corresponding to the folding
 513 tropopause.

514 Previous research suggested that cyclonic flow is preferred near double tropopauses
 515 [e.g. *Randel et al., 2007a; Wang and Polvani, 2011*]. The destabilization/stretching mecha-
 516 nism can potentially explain this preference. When an air parcel is adiabatically stretched/destabilized,
 517 the pseudo-density $\sigma = \frac{1}{g} \frac{\partial p}{\partial \theta}$ increases. To conserve $PV = (f + \zeta) / \sigma$, absolute vortic-
 518 ity $f + \zeta$ has to increase. For baroclinic waves, this increase is a result of an increase in

519 relative vorticity ζ rather than f (not shown). Therefore, relative vorticity is likely to be
 520 positive in the presence of adiabatic stabilization.

521 In the eddy lifecycle simulations, double tropopauses only enhance the equatorward
 522 stratosphere-to-troposphere exchange, which is inconsistent with the dominant poleward
 523 advection associated with double tropopauses in the observations. The reason for the
 524 equatorward enhancement in our idealized simulation may be that the double tropopauses
 525 only occur in the equatorward lobe of the breaking wave where the exchange across the
 526 tropopause is dominated by an equatorward flux (not shown). However, in observations
 527 double tropopauses occur in both poleward and equatorward lobes of wave breaking (Fig.
 528 6) and poleward advection is more favorable for double tropopauses [e.g. *Randel et al.*,
 529 2007a; *Pan et al.*, 2009; *Castanheira and Gimeno*, 2011]. Therefore, double tropopauses in
 530 the observations may actually predominantly enhance poleward mixing of tropospheric air
 531 into the stratosphere. More research is needed to test this.

532 The dominant mechanism responsible for double tropopause formation during Rossby
 533 wave breaking events also appears to be different between the eddy lifecycle simulations
 534 and the observations. In particular, differential advection contributes to the dominant dou-
 535 ble tropopause formation near the poleward lobe of anticyclonic wave breaking while in
 536 the eddy lifecycle simulation vertical stretching contributes to the double tropopause for-
 537 mation in its equatorward lobe. We suggest such difference in the wave breaking charac-
 538 teristics may be related to very different jet configurations in the real atmosphere and in
 539 the idealized lifecycle simulation.

540 Our study focuses on adiabatic mechanisms of double tropopause formation by syn-
 541 optic waves. However, there are certainly other mechanisms that are relevant. One exam-
 542 ple is mean advection. Specifically, we depict the advection we are interested in by equiv-
 543 alent latitude anomaly ϕ_a , which excludes the influence of mean advection. *Birner* [2010]
 544 showed that the climatological mean meridional structure of N^2 exhibits slight folding
 545 in the subtropics and mean advection contributes to this folding. Another component we
 546 neglect is the diabatic change in thermal stratification by radiative processes involving
 547 ozone and water vapor. Studies have shown their role in forming a TIL [e.g. *Randel et al.*,
 548 2007b; *Ferreira et al.*, 2016; *Kunkel et al.*, 2016]. It is possible these diabatic processes
 549 can influence the formation of double tropopauses directly, or indirectly by their ability to
 550 modify TIL. In addition, as ozone and water vapor distributions near the tropopause are

551 mainly determined by transport and mixing, their feedbacks on thermal stratification are
 552 likely coupled to adiabatic processes such as differential advection. More research is war-
 553 ranted to unfold these interactions.

554 Among the results, perhaps the most striking one is how much double tropopauses
 555 can enhance the stratosphere-to-troposphere exchange in idealized eddy lifecycles which
 556 are themselves strong in transport and mixing to begin with [e.g. *Polvani and Esler, 2007*].
 557 Given the ubiquitousness of double tropopauses in the observations, they likely play a sig-
 558 nificant role in the stratosphere-troposphere exchange and account for its variability at
 559 least on synoptic time scales. Our results regarding their linkage to wave breaking and
 560 their formation mechanisms may then help advance understanding of the variability of the
 561 global stratosphere-troposphere exchange.

562 **A: Quantification of ϕ_a^{diff} and ϕ_a^{mean}**

563 To quantify the advection patterns corresponding to each GPS profile, ERA-Interim
 564 data is used to calculate the equivalent latitude anomaly profile $\phi_a(\theta)$ colocated with
 565 the GPS profiles. By summing and subtracting ϕ_a in the vertical direction, we isolate
 566 two aspects of the advection patterns – differential advection (ϕ_a^{diff}) and mean advection
 567 (ϕ_a^{mean}), respectively. Differential advection represents the shear of advection in merid-
 568 ional plane and is calculated as:

$$\phi_a^{diff} = \frac{\phi_a(380K) - \phi_a(\theta_{TP})}{380K - \theta_{TP}} \quad (\text{A.1})$$

569 where θ_{TP} is the potential temperature θ at the first tropopause. 380K is used here for
 570 an upper level above the first tropopause. The result is not sensitive as we vary this value
 571 between 380K and 450K (not shown).

572 The mean advection represents the average advection direction above the lowest
 573 tropopause and is calculated as:

$$\phi_a^{mean} = \frac{\phi_a(380K) + \phi_a(\theta_{TP})}{2} \quad (\text{A.2})$$

574 Positive values denote poleward mean advection and negative values denote equatorward
 575 mean advection.

576 Acknowledgments

577 This work was supported by the Climate and Large-scale Dynamics Program of the Na-
 578 tional Science Foundation under Grant 1419818. The COSMIC GPS data is provided
 579 publicly by UCAR CDAAC (<http://cdaac-www.cosmic.ucar.edu/cdaac/products.html>). The
 580 ERA-Interim data is provided publicly by ECMWF data center ([http://apps.ecmwf.int/datasets/data/interim-
 581 full-daily/](http://apps.ecmwf.int/datasets/data/interim-full-daily/)). We also thank Thomas Birner, Laura Pan, William Randel, and Marty Singh
 582 for helpful discussions and comments.

583 References

- 584 Añel, J. A., J. C. Antuna, L. de la Torre, J. M. Castanheira, and L. Gimeno (2008), Cli-
 585 matological features of global multiple tropopause events, *Journal of Geophysical Re-
 586 search: Atmospheres*, 113(D7).
- 587 Añel, J. A., L. de la Torre, and L. Gimeno (2012), On the origin of the air between multi-
 588 ple tropopauses at midlatitudes, *The Scientific World Journal*, 2012.
- 589 Birner, T. (2006), Fine-scale structure of the extratropical tropopause region, *Journal of
 590 Geophysical Research: Atmospheres*, 111(D4).
- 591 Birner, T. (2010), Residual circulation and tropopause structure, *J. Atmos. Sci.*, 67(8),
 592 2582–2600.
- 593 Birner, T., A. Dörnbrack, and U. Schumann (2002), How sharp is the tropopause at mid-
 594 latitudes?, *Geophysical research letters*, 29(14).
- 595 Birner, T., D. Sankey, and T. Shepherd (2006), The tropopause inversion layer in models
 596 and analyses, *Geophysical research letters*, 33(14).
- 597 Butchart, N., and E. E. Remsberg (1986), The area of the stratospheric polar vortex as a
 598 diagnostic for tracer transport on an isentropic surface, *J. Atmos. Sci.*, 43(13), 1319–
 599 1339.
- 600 Castanheira, J., and L. Gimeno (2011), Association of double tropopause events with baro-
 601 clinic waves, *Journal of Geophysical Research: Atmospheres*, 116(D19).
- 602 Castanheira, J., T. Peevey, C. Marques, and M. Olsen (2012), Relationships between
 603 brewer-dobson circulation, double tropopauses, ozone and stratospheric water vapour,
 604 *Atmospheric Chemistry and Physics*, 12(21), 10,195–10,208.
- 605 Dee, D., S. Uppala, A. Simmons, P. Berrisford, P. Poli, S. Kobayashi, U. Andrae, M. Bal-
 606 maseda, G. Balsamo, P. Bauer, et al. (2011), The ERA-Interim reanalysis: Configuration
 607 and performance of the data assimilation system, *Quarterly Journal of the Royal Meteo-*

- 608 *rological Society, 137(656), 553–597.*
- 609 Ferreira, A. P., J. M. Castanheira, and L. Gimeno (2016), Water vapour stratification
610 and dynamical warming behind the sharpness of the earth’s midlatitude tropopause,
611 *Quarterly Journal of the Royal Meteorological Society, 142(695), 957–970*, doi:
612 10.1002/qj.2697.
- 613 Forster, F., M. Piers, and K. P. Shine (1997), Radiative forcing and temperature trends
614 from stratospheric ozone changes, *Journal of Geophysical Research: Atmospheres,*
615 *102(D9), 10,841–10,855.*
- 616 Hegglin, M. I., and T. G. Shepherd (2009), Large climate-induced changes in ultraviolet
617 index and stratosphere-to-troposphere ozone flux, *Nature Geoscience, 2(10), 687–691.*
- 618 Homeyer, C. R., L. L. Pan, S. W. Dorsi, L. M. Avallone, A. J. Weinheimer, A. S. O’Brien,
619 J. P. DiGangi, M. A. Zondlo, T. B. Ryerson, G. S. Diskin, et al. (2014), Convective
620 transport of water vapor into the lower stratosphere observed during double-tropopause
621 events, *Journal of Geophysical Research: Atmospheres, 119(18).*
- 622 Kochanski, A. (1955), Cross sections of the mean zonal flow and temperature along 80° w,
623 *Journal of Meteorology, 12(2), 95–106.*
- 624 Kunkel, D., P. Hoor, and V. Wirth (2016), The tropopause inversion layer in baroclinic
625 life-cycle experiments: the role of diabatic processes, *Atmospheric Chemistry and*
626 *Physics, 16(2), 541–560.*
- 627 Liou, Y.-A., A. G. Pavelyev, S.-F. Liu, A. A. Pavelyev, N. Yen, C.-Y. Huang, and C.-J.
628 Fong (2007), Formosat-3/cosmic gps radio occultation mission: Preliminary results,
629 *IEEE Transactions on Geoscience and Remote Sensing, 45(11), 3813–3826.*
- 630 Liu, C., X. Ren, and X. Yang (2014), Mean flow-storm track relationship and Rossby
631 wave breaking in two types of El-Niño, *Adv. Atmos. Sci., 31(1), 197–210.*
- 632 Pan, L. L., W. J. Randel, J. C. Gille, W. D. Hall, B. Nardi, S. Massie, V. Yudin, R. Khos-
633 ravi, P. Konopka, and D. Tarasick (2009), Tropospheric intrusions associated with the
634 secondary tropopause, *Journal of Geophysical Research: Atmospheres, 114(D10)*, doi:
635 10.1029/2008JD011374, d10302.
- 636 Peevey, T., J. Gille, C. Homeyer, and G. Manney (2014), The double tropopause and its
637 dynamical relationship to the tropopause inversion layer in storm track regions, *Journal*
638 *of Geophysical Research: Atmospheres, 119(17).*
- 639 Peevey, T. R., J. C. Gille, C. E. Randall, and A. Kunz (2012), Investigation of double
640 tropopause spatial and temporal global variability utilizing high resolution dynamics

- 641 limb sounder temperature observations, *Journal of Geophysical Research: Atmospheres*,
642 *117*(D1).
- 643 Polvani, L. M., and J. G. Esler (2007), Transport and mixing of chemical air masses
644 in idealized baroclinic life cycles, *Journal of Geophysical Research: Atmospheres*,
645 *112*(D23), doi:10.1029/2007JD008555, d23102.
- 646 Randel, W. J., D. J. Seidel, and L. L. Pan (2007a), Observational characteristics of
647 double tropopauses, *Journal of Geophysical Research: Atmospheres*, *112*(D7), doi:
648 10.1029/2006JD007904, d07309.
- 649 Randel, W. J., F. Wu, and P. Forster (2007b), The extratropical tropopause inversion layer:
650 Global observations with GPS data, and a radiative forcing mechanism, *Journal of the*
651 *Atmospheric Sciences*, *64*(12), 4489–4496.
- 652 Riese, M., F. Ploeger, A. Rap, B. Vogel, P. Konopka, M. Dameris, and P. Forster (2012),
653 Impact of uncertainties in atmospheric mixing on simulated utls composition and re-
654 lated radiative effects, *Journal of Geophysical Research: Atmospheres*, *117*(D16).
- 655 Schwartz, M., G. Manney, M. Hegglin, N. Livesey, M. Santee, and W. Daffer (2015), Cli-
656 matology and variability of trace gases in extratropical double-tropopause regions from
657 mls, hirdls, and ace-fts measurements, *Journal of Geophysical Research: Atmospheres*,
658 *120*(2), 843–867.
- 659 Seidel, D. J., and W. J. Randel (2006), Variability and trends in the global tropopause esti-
660 mated from radiosonde data, *Journal of Geophysical Research: Atmospheres*, *111*(D21).
- 661 Shapiro, M. (1980), Turbulent mixing within tropopause folds as a mechanism for the ex-
662 change of chemical constituents between the stratosphere and troposphere, *J. Atmos.*
663 *Sci.*, *37*(5), 994–1004.
- 664 Solomon, S., K. H. Rosenlof, R. W. Portmann, J. S. Daniel, S. M. Davis, T. J. Sanford,
665 and G.-K. Plattner (2010), Contributions of stratospheric water vapor to decadal changes
666 in the rate of global warming, *Science*, *327*(5970), 1219–1223.
- 667 Son, S.-W., N. F. Tandon, and L. M. Polvani (2011), The fine-scale structure of the global
668 tropopause derived from cosmic gps radio occultation measurements, *Journal of Geo-*
669 *physical Research: Atmospheres*, *116*(D20).
- 670 U.S. Environmental Protection Agency (U.S. EPA) (2006), Air quality criteria for ozone
671 and related photochemical oxidants (2006 final).
- 672 Wang, S., and L. M. Polvani (2011), Double tropopause formation in idealized baroclinic
673 life cycles: The key role of an initial tropopause inversion layer, *Journal of Geophysical*

674 *Research: Atmospheres*, 116(D5), doi:10.1029/2010JD015118, d05108.

675 Wickert, J., G. Beyerle, R. König, S. Heise, L. Grunwaldt, G. Michalak, C. Reigber, and
676 T. Schmidt (2005), Gps radio occultation with champ and grace: A first look at a new
677 and promising satellite configuration for global atmospheric sounding, *Annales Geophys-*
678 *icae*, 23(3), 653–658, doi:10.5194/angeo-23-653-2005.

679 Wirth, V. (2001), Cyclone–anticyclone asymmetry concerning the height of the thermal
680 and the dynamical tropopause, *Journal of the atmospheric sciences*, 58(1), 26–37.

681 World Meteorological Organization, W. (1957), A three-dimensional science: Second ses-
682 sion of the commission for aerology, *WMO Bull*, 4(2), 134–138.